

Land Subsidence Monitoring and Analysis in Heifei Based on Sentinel-1A Data

Kai Xu,^{1,2*} Siyuan Liu,¹ and Chengcheng Fan^{3,4**}

¹School of Internet, Anhui University, Heifei 230039, China

²Earth Observation Research and Development Center, 38th Institute of China Electronics Science Corporation, Heifei 230031, China

³Shanghai Engineering Center for Microsatellites, Shanghai 201210, China

⁴Innovation Academy for Microsatellites of CAS, Shanghai 201210, China

(Received June 1, 2023; accepted October 5, 2023)

Keywords: PSInSAR, Sentinel-1A, SBAS, urban deformation, metro protection zone

Urban land subsidence is one of the important limiting factors for urban development, and strengthening the monitoring of urban surface subsidence contributes to long-term urban planning and construction needs. As a subcentral city in the Yangtze River Delta region of China, it is particularly important for Heifei to enhance the monitoring of surface subsidence. In this study, the persistent scatterer interferometric synthetic aperture radar (PS-InSAR) and small baseline subset (SBAS) techniques were used to process 139 scenes of Sentinel-1A SAR satellite ascending orbit data covering the central urban area of Hefei from July 2015 to July 2020, obtaining subsidence information for the region. The results show that the overall urban area of Heifei is relatively stable, but there are certain deformation trends in local areas. Four regions with obvious deformation were selected for the in-depth analysis of their deformation time series. The experimental study in this paper demonstrates that the PS-InSAR and SBAS techniques can achieve the accurate monitoring of large-scale ground subsidence in urban areas, ensuring the safety of buildings and their surrounding environments, and providing information support for urban security maintenance monitoring.

1. Introduction

With the rapid development of China's social economy and the continuous acceleration of urban modernization, land subsidence has become the biggest threat to the rapid development of cities and the lives and properties of residents.^(1,2) Currently, more than 150 countries around the world are facing the risk of urban land subsidence, as urban infrastructures such as buildings, highways, airports, and subways are often damaged by changes in the surface space of these cities.^(3,4) The comprehensive effect of human activities and geological factors is the main cause of land subsidence.⁽⁵⁾ Land subsidence caused by geological factors is the result of geological structures, earthquakes, or the consolidation and compression of loose surface layers under the influence of gravity. Urban land subsidence is mainly caused by human activities, including the

*Corresponding author: e-mail: kaiXu@ahu.edu.cn

**Corresponding author: e-mail: fance@microstate.com

<https://doi.org/10.18494/SAM4546>

excessive exploitation of underground resources such as groundwater, minerals, and natural gas, as well as the construction of high-rise buildings and underground engineering. To ensure the stability of the surface and prevent the occurrence of ground collapse, it has become important and practical to conduct the large-scale, high-precision, and long-term ground detection of the urban surface.^(6–8)

Traditional methods for detecting land subsidence, such as the use of the global positioning system, precise leveling measurements, and total station surveys, are affected by various factors such as terrain and equipment installation. Measurement stations are usually sparsely distributed, making the long-term maintenance of observation points difficult, time-consuming, labor-intensive, and costly; thus, they are unable to meet the needs of large-scale, real-time, and high-precision surface deformation detection. In recent years, the Interferometric Synthetic Aperture Radar (InSAR) has been widely applied in terrain mapping, surface deformation monitoring, and other fields owing to its advantages of all-weather, all-time coverage, wide area coverage, and high spatial resolution. It has also found extensive application in urban land subsidence monitoring. InSAR-based measurements, relying on the phase information of SAR images, as well as a series of other improved time series InSAR methods, including Differential InSAR, Persistent Scatterer InSAR (PS-InSAR), Small Baseline Subset InSAR (SBAS-InSAR),⁽⁹⁾ and Multiple Aperture Interferometry (MAI) techniques, are based on the principle of time-to-distance imaging. They utilize the complex conjugate multiplication of SAR complex images to obtain interferograms and calculate the path difference between two radar waves, thus monitoring one-dimensional small deformations along the line-of-sight (LOS) direction of the radar wave.⁽¹⁰⁾ Theoretically, the measurement accuracy can reach the millimeter level. Applying InSAR technology to the study of urban land subsidence detection in China is of great significance for urban planning and governance and for ensuring urban economic development.

In this study, we focus on the main urban area of Hefei as the research area and employ the PS-InSAR technique along with the SBAS processing method. We utilize a dataset consisting of 139 Sentinel-1A single-looking complex (SLC) images covering the period from July 2015 to July 2020 to conduct a comprehensive five-year deformation monitoring experiment in the main urban area of Hefei. The main objective of this research is to assess and demonstrate the potential application of InSAR technology in the field of urban land subsidence monitoring.

2. Principle of PSInSAR Technique

The PSInSAR technique utilizes a time series of synthetic aperture radar (SAR) images acquired at different time intervals in the same area. Assuming there are $M + 1$ SAR radar images from different time periods in the study area, one image is selected as the master image based on experimental requirements, while the remaining M SAR images serve as slave images. These images undergo registration and interferometric processing, with an external Digital Elevation Model (DEM)⁽¹¹⁾ introduced to remove terrain phase effects. This process results in M pairs of interferometric image sets, yielding M sets of differential data. By constructing a model based on the obtained Permanent Scatterer (PS) points, the subsidence results for the study area are calculated.^(12–16) In this equation, the phase $\Delta\phi_i$ for the i th phase can be represented as

$$\Delta\varphi_i = \varphi_{\text{def}_i} + \varphi_{\text{topo}_i} + \varphi_{\text{atm}_i} + \varphi_{\text{noise}_i}. \quad (1)$$

Here, φ_{def_i} represents the deformation phase in the LOS direction caused by surface deformation during the imaging period; φ_{topo_i} accounts for the terrain phase introduced by external DEM errors; φ_{atm_i} corresponds to the phase delay caused by atmospheric disturbances during the imaging period; φ_{noise_i} denotes the noise phase, including spatial decorrelation noise, temporal decorrelation noise, system noise, and other types of noise, following a Gaussian distribution. The processing flow is illustrated in Fig. 1.

3. Principle of SBAS Technique

The SBAS-InSAR technique employs a time-series analysis approach using a combination of interferograms derived from multiple image pairs with short baselines.⁽¹⁷⁾ High-quality interferograms are selected by applying a temporal baseline threshold (TBT) and a perpendicular baseline threshold (PBT),⁽¹⁸⁾ which effectively filter out interferograms with poor quality. To optimize spatial decorrelation, the temporal and spatial baselines between differential interferograms should be minimized, enabling the connection of all pairs with short baselines

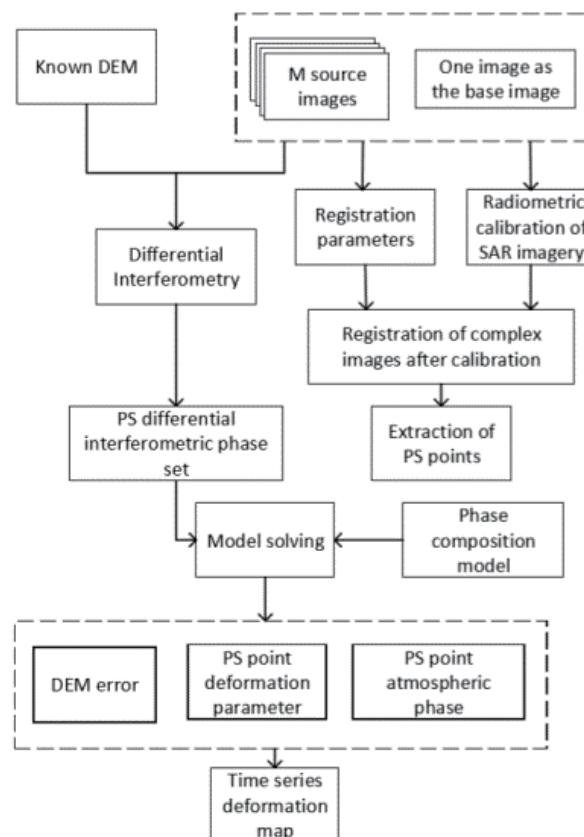


Fig. 1. PS-InSAR processing flow.

within the set. Isolated SAR data with large spatial baselines are also connected, accelerating the sampling rate of observation data. Ultimately, several smaller subsets can be formed within the existing SAR image dataset, where both temporal and spatial baselines fall within the designated threshold range, all linked through a master image.⁽¹⁹⁾

Assuming there are $M + 1$ SAR images covering the study area, acquired at times t_0, t_1, \dots, t_m , N sets of interferometric pairs can be obtained through freely combined image pairing:

$$\frac{M+1}{2} \leq N \leq M \frac{M+1}{2}. \quad (2)$$

For a pair of SAR images acquired at times t_a and t_b ($t_b > t_a$), the interferogram generated from these images is the i th interferogram. The interferometric phase $\phi(i, \beta)$ of a specific interferometric pixel β in this interferogram is calculated as

$$\phi_{(i,\beta)} = \phi_{(t_b,\beta)} - \phi_{(t_a,\beta)} \approx \frac{4\pi}{\lambda} [d(t_b, \beta) - d(t_a, \beta)]. \quad (3)$$

Here, $d(t_b, \beta)$ and $d(t_a, \beta)$ are the deformation components along the radar LOS direction at times t_b and t_a , respectively. $d(t_b, \beta)$ ($i = 1, \dots, M$) represents the accumulated deformation time series, $\Phi(t_i, \beta)$ is the corresponding phase, and the unwrapped phase is calculated as

$$\phi(t_i, \beta) \approx \frac{4\pi d(t_i, \beta)}{\lambda}. \quad (4)$$

Assuming $\Phi^T = [\Phi(t_1), \Phi(t_2), \dots, \Phi(t_M)]$ is a vector set composed of phases corresponding to a specific pixel in different moments of SAR images,⁽²⁰⁾ the corresponding interferometric phase vector set is

$$\Delta\phi^T = [\Delta\phi(t_1), \Delta\phi(t_2), \dots, \Delta\phi(t_M)]. \quad (5)$$

The time series of the master and slave images are represented as $IE = [IE_1, IE_2, \dots, IE_N]$ and $IS = [IS_1, IS_2, \dots, IS_M]$, respectively. If $IE_i > IS_i$ ($i = 1, \dots, N$), then the interferometric phase of the i th interferogram is

$$\phi_i = \phi_{t_{IE_i}} - \phi_{t_{IS_i}} \quad (i = 1 \dots N). \quad (6)$$

From the above equation, the corresponding matrix expression is

$$A\phi = \sigma\phi, \quad (7)$$

where AN^*M is the coefficient matrix, with each row corresponding to each interferogram and each column corresponding to each SAR image. When $N \geq M$, the least-squares solution can be directly obtained:

$$\hat{\phi} = (A^T A)^{-1} A^T \sigma \phi. \quad (8)$$

When $N < M$, ATA is a non-singular matrix.⁽²¹⁾ In this case, the solution of Φ in the least-norm sense can be found, leading to

$$V^T = \left[V_1 = \frac{\phi_1 - \phi_0}{t_1 - t_0}, V_2 = \frac{\phi_2 - \phi_1}{t_2 - t_1}, \dots, V_M = \frac{\phi_M - \phi_{M-1}}{t_M - t_{M-1}} \right]. \quad (9)$$

Substituting this into the previous equation yields

$$\sum_{k=IS_i+1}^{IE_i} V_k = \sigma \phi_i (i = 1, 2, \dots, N). \quad (10)$$

Consequently, the matrix budget expression can be transformed into

$$BV = \sigma \phi, \quad (11)$$

where BN^*M is the coefficient matrix. When $IS_i+1 < k < IE_i$, $B(i, k) = t_{k+1} - t_k$ ($i = 1, 2, \dots, N$); otherwise, $B(i, k) = 0$. By utilizing the SVD decomposition method, the least-norm solution of the velocity vector can be obtained. Finally, integrating the velocities within each time interval yields the corresponding deformation components.^(22,23) The SBAS processing workflow is depicted in Fig. 2.

4. Study Area Overview

4.1 Study area overview

The study area is the central urban area of Hefei City, with a coverage area of approximately $12 \times 20 \text{ km}^2$. Most areas have an altitude between 15 and 80 m, with an average altitude of 20–40 m. Hefei, as a subcentral city in the Yangtze River Delta urban agglomeration, has experienced rapid socioeconomic development in recent years. Monitoring and analyzing the land subsidence caused by urban construction in Hefei City are of great significance.

4.2 Data sources

In this study, 139 scenes of ascending orbit interferometric wide swath (IW) SLC data covering the central urban area of Hefei were obtained from Sentinel-1A. The data span from

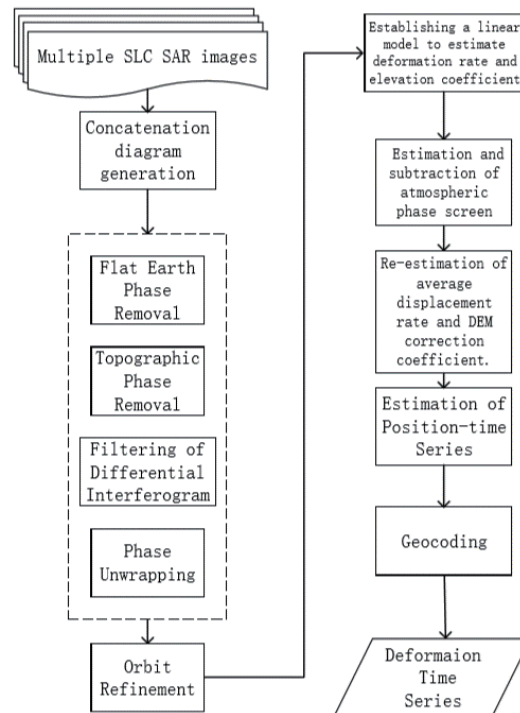


Fig. 2. SBAS processing flow.

July 2015 to July 2020. The slant range resolution of the data is approximately $2.3 \times 13.3 \text{ m}^2$ (range \times azimuth), and the average incidence angle is around 39.3° . Precise Orbit Ephemerides data, with an accuracy higher than 5 cm, were used as the orbit information, which meets the requirements for InSAR data processing. The DEM data used in this study is the Shuttle Radar Topographic Mission Global 1, with a resolution of 30 m, obtained from airborne radar terrain mapping. The detailed research data parameters are shown in Table 1.

5. Experimental Results and Discussion

5.1 PS-InSAR processing results

Using the data from January 15, 2018 as the master image, we performed the PS-InSAR processing with a spatial baseline threshold of 180 m and a temporal threshold of 840 days, resulting in the spatio-temporal baseline distribution of the interferometric pairs as shown in Fig. 3.

In this study, the PS point selection method combining the amplitude dispersion threshold and spectral coherence coefficient was employed. A total of 180381 PS measurement points were obtained within the 240 square kilometers of the central urban area of Heifei City, with an average PS point density of 751.6 points per square kilometer. From the point density distribution, the northern part of the study area exhibited a significantly higher density than the southern

Table 1
Research data parameters.

Sentinel-1A Satellite Parameters	Value
Acquisition Time Range	2015.7–2020.7
Data Volume/Scene	139
Ascending/Descending	Ascending
Imaging Mode	Interferometric Wide (IW)
Polarization Mode	VV
Incidence Angle (°)	39.3
Resolution/m	2.3×13.3 (Range \times Azimuth)
Repeat Cycle/d	12

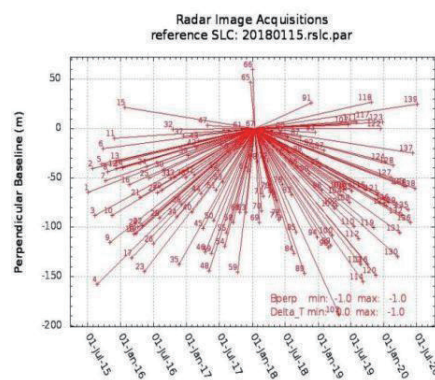


Fig. 3. (Color online) Spatio-temporal baseline of Sentinel-1 data interference.

region. This can be attributed to the dense urban construction in the northern part, which has more high-coherence point targets. In contrast, the southern region has a relatively higher vegetation coverage, especially in the southeast where there is less urban development, resulting in a lack of valid measurement signals in certain localized areas. (Comprehensive coverage can be achieved by combining the SBAS technique with PSinSAR.) The specific distribution of deformation rates is shown in Fig. 4.

According to the deformation rate distribution in Fig. 4, the overall stability of the urban area in Heifei can be observed, with LOS annual average deformation rates ranging from -5 to 5 mm/year. In particular, the northeastern region of the study area shows minimal deformation and is considered the most stable. Localized areas in the central-southern part of the study area exhibit certain deformation trends, represented by regions A, B, C, and D in the figure. These regions will be further analyzed in subsequent sections. The study area includes several important transportation lines, including parts of Metro Line 1, parts of Metro Line 2, the central section of Metro Line 3, and certain high-speed railway lines within Heifei. Among them, Metro Lines 2 and 3 exhibit overall stability without passing through significant deformation areas, while a portion of Metro Line 1 in the southern segment shows deformation, as exemplified by region D. Additionally, there are indications of deformation along the railway lines within Heifei, including Heifei South Station. The deformation velocity distribution map clearly shows a linear distribution of PS points along the railway lines, which align well with the railway tracks,

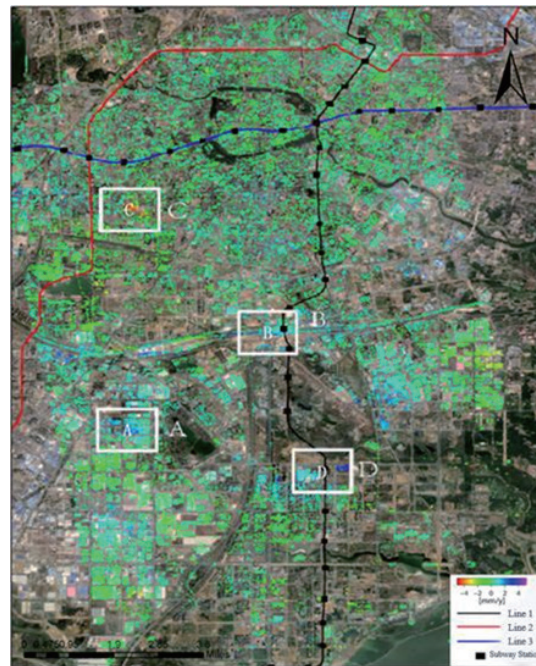


Fig. 4. (Color online) Distribution of deformation rates in Hefei urban area from July 2015 to July 2020.

indicating that the PSInSAR processing of Sentinel data can provide monitoring results with relatively high spatial resolution, meeting the requirements for subsidence monitoring in urban areas.

5.2 SBAS processing results

The data acquired on July 9, 2019 was selected as the master image. The spatial baseline threshold was set at 2% of the critical baseline, and the temporal baseline threshold was set at 120 days. On the basis of these criteria, a total of 139 pairs of interferometric images were generated, as shown in Fig. 5.

After phase unwrapping and removing the effects of flat-earth, DEM errors, orbit errors, and atmospheric effects, the surface deformation of the study area was computed. The LOS average deformation in the urban area ranged mostly from -10 to 10 mm/year, as depicted in Fig. 6. In the deformation map, colder colors represent upward deformation along the LOS direction, while warmer colors represent downward subsidence, which aligns with the deformation trend obtained through the PS-InSAR processing.

Overall, the annual average deformation rate results obtained from both techniques show good agreement, indicating a high level of consistency between the two methods. Although there are slight differences observed in the image results, both methods are considered reliable for monitoring land subsidence in urban areas. The use of small baseline distances in the SBAS approach helps to avoid spatial decorrelation and reduces the effect of topography on the interferograms. The resulting deformation map shows a greater continuity in spatial coverage than does the PS-InSAR method.

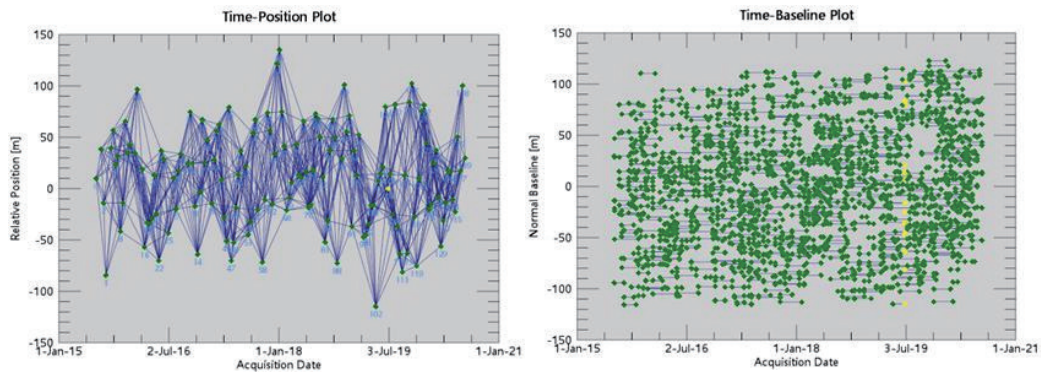


Fig. 5. (Color online) Interferogram connectivity graph and spatiotemporal baseline distribution.

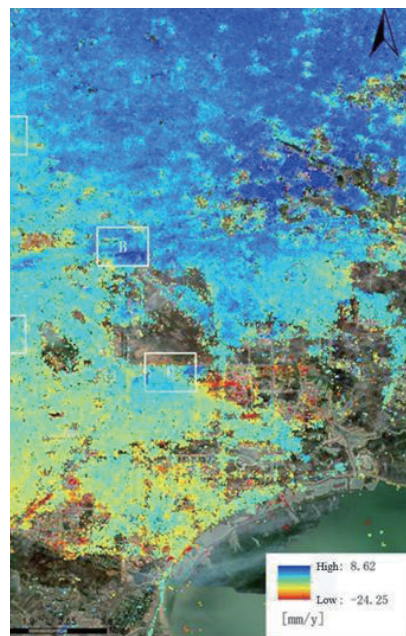


Fig. 6. (Color online) Annual mean deformation rate of SBAS LOS.

5.3 Spatiotemporal analysis of key deformation areas

To further analyze the distribution of subsidence velocities in the urban area of Heifei from July 2015 to July 2020, we selected four representative deformation areas (highlighted by white boxes A, B, C, and D in Fig. 4) for comparative analysis. The aim was to validate the accuracy of the results obtained from both PS-InSAR and SBAS with small baselines and to investigate the causes of deformation in these areas.

5.3.1. Anhui Jiatong Tire Factory area

From Fig. 4, it can be observed that Area A exhibits positive deformation signals, and optical image comparison reveals that this area corresponds to the Jiatong Tire Factory in Anhui. To further analyze the deformation characteristics and evolution of this area, a specific point within Area A was selected to analyze its deformation time series, as shown in Fig. 7. The deformation time series reveals that the LOS direction in this area demonstrates a linear deformation trend with a pronounced periodic deformation pattern. It shows an upward expansion (positive deformation) during the summer and a downward contraction (negative deformation) during the winter, with vibration amplitudes ranging from -20 to $+20$ mm. This phenomenon is attributed to the thermal expansion and contraction of the steel structure in the tire factory, causing cyclic deformation in response to seasonal temperature variations. This observation confirms the high precision of InSAR technology in urban areas, which is capable of accurately capturing deformations caused by temperature-induced changes in steel frame structures.

The consistency between the subsidence trends obtained from SBAS and PS-InSAR technologies confirms their accuracy to a certain extent. Trend analysis further verifies the seasonal temperature variations in the steel frame structure of the tire factory. Considering the contamination of periodic signals in the linear deformation trend, we performed a simple modeling using a sine function to estimate the effects of thermal expansion and contraction. The resulting linear deformation trend time series after removing this component is shown in Fig. 8, indicating a linear deformation trend of approximately 1.6 mm/year in the tire factory area. However, since the simple trigonometric function fitting does not precisely capture the changes in the thermal expansion and contraction of the steel frame structure, the accuracy of the

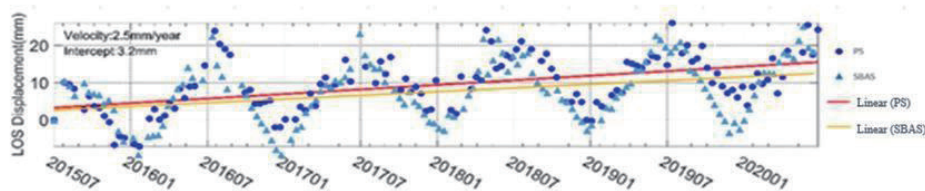


Fig. 7. (Color online) Deformation time series from July 2015 to July 2020 in Jiatong Tire Factory area of Anhui Province.

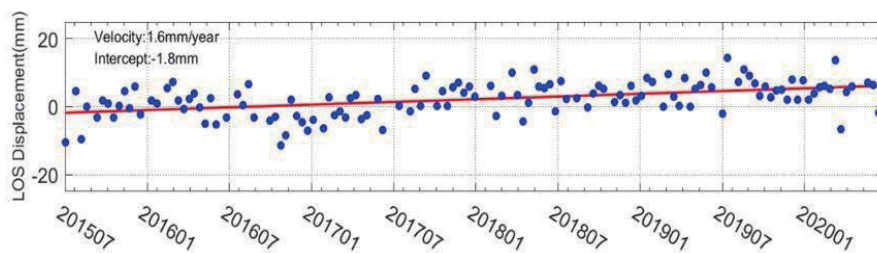


Fig. 8. (Color online) Time series of regional linear deformation trend of Jiatong Tire Factory in Anhui Province.

deformation trend time series is affected. Therefore, in future studies, it is necessary to establish a rigorous deformation model for the thermal expansion and contraction of the steel frame structure on the basis of temperature data, in order to more accurately remove the periodic signal.

5.3.2. Hefei South Station

From Fig. 4, it can be observed that Area B exhibits positive deformation signals, and optical mapping reveals that this area corresponds to Hefei South Station, a high-speed railway station. Similarly, to further analyze the deformation characteristics and evolution of this area, a specific point within Area B was selected to analyze its deformation time series, as shown in Fig. 9. The results indicate that Hefei South Station has also experienced thermal expansion and contraction due to temperature variations in its steel frame structure, with a LOS amplitude range of approximately ± 25 mm. It can be observed that there is a significant fluctuation during the summer, and the subsidence trend shown by PS-InSAR and SBAS in the LOS direction is generally consistent. Furthermore, note that starting from 2017, there is a slight uplift during the winter and summer compared with the same period in the previous year. Since there are no new buildings observed in the vicinity, it can be inferred that this is due to the construction of Metro Line 5. During the construction and operation of the subway, the initial stage of subsidence is small, but as concrete is poured, the base rebounds and undergoes uplift deformation, resulting in ground uplift phenomena. By using the trigonometric function fitting to remove the periodic signal, the linear deformation trend time series of this area was obtained, as shown in Fig. 10. The results indicate a stable deformation trend of approximately 2.5 cm/year in this area, which requires further observation of its deformation trend.

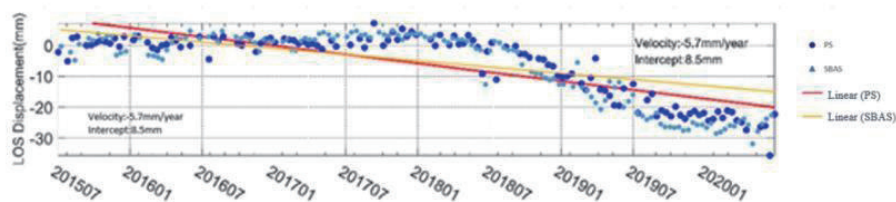


Fig. 9. (Color online) Deformation time series of Hefei South Railway Station from July 2015 to July 2020.

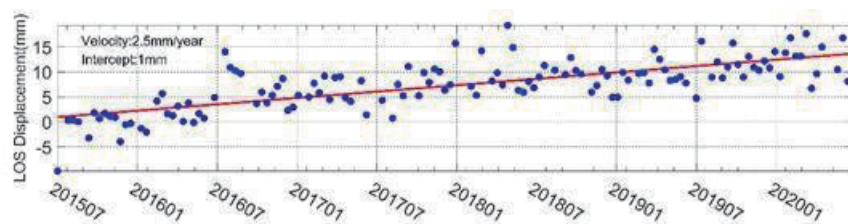


Fig. 10. (Color online) Time series of linear deformation trend in Hefei South Railway Station.

5.3.3. University college

Area C exhibits negative deformation signals, mainly corresponding to the university college. Figure 11 shows the deformation time series of this area from July 2015 to July 2020. From the time series, it can be observed that the deformation in the LOS direction fluctuated around zero from 2015 to the first half of 2018, indicating a relatively stable state during that period. However, a rapid subsidence signal was obtained from June 2018 to September 2019, with the deformation quickly changing from zero to -20 mm, followed by a relatively stable state up to the present.

Using optical imagery from Tianditu, as shown in Fig. 12, we observed that there were significant changes in the buildings on the university campus during the period from July 2018 to September 2019. This corresponds precisely to the rapid deformation period revealed by InSAR monitoring. It is preliminarily inferred that this deformation is due to geological subsidence caused by changes in the campus planning. This experiment further demonstrates the capability of InSAR technology to accurately capture surface deformation information.

5.3.4. Anhui Geological Information Museum area

Area D is located near the No. 1 subway line, with the main building being the Anhui Geological Information Museum (Fig. 13). The results indicate a LOS deformation trend of approximately 4 mm/year in this area. As shown in Fig. 14, through the time series analysis, it is observed that this area also exhibits a certain periodic deformation trend. However, compared with the previous cases A and B, the signal in this area is more complex. The periodic signal was more pronounced before 2019 but disappeared afterward. Before 2019, the subsidence remained around ± 10 mm/year, and afterward, it showed a fluctuating pattern and eventually stabilized. According to investigations, the Anhui Geological Information Museum is located on Jinxiu Avenue, near the Shiwuli River, with mostly farmland in the vicinity and the ongoing construction of Luzhou Avenue. It is speculated that the subsidence may be caused by the irrigation of farmland and the extraction of groundwater. Further analysis is required to combine these results with actual conditions.

5.4 Cross-validation

Randomly selecting 10000 validation points within the study area, we expanded each point outward with a radius of 30 m to find the nearest PS points within the radius. The LOS annual average subsidence rates obtained from both methods were cross-validated and analyzed. If no PS points were found within the radius, the validation point was considered invalid. In the end, 3488 PS and 4277 SBAS validation points were obtained.⁽²⁴⁾ After statistical analysis, a normal distribution curve was obtained, as shown in Fig. 15. The relative error between the two inversion results was 1.5 mm/year, which falls within the accuracy range of 5 mm/year. To demonstrate the consistency of the results from both methods more intuitively, a linear fit was performed on the valid validation points, resulting in a linear relationship of 0.95, as shown in

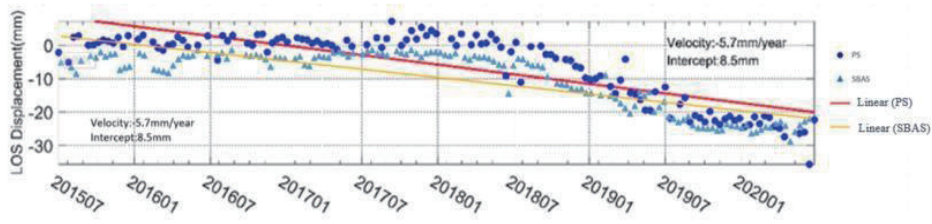


Fig. 11. (Color online) Deformation time series of college area from July 2015 to July 2020.

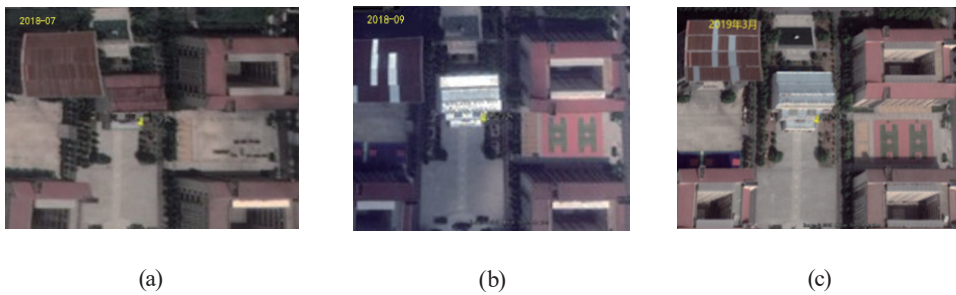


Fig. 12. (Color online) Optical remote sensing image of university college: (a) July 2018, (b) September 2018, and (c) February 2019.



Fig. 13. (Color online) Satellite map of Anhui Geological Information Museum.

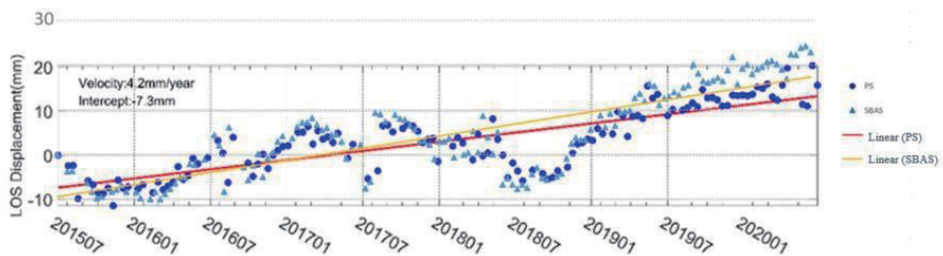


Fig. 14. (Color online) Deformation time series of Anhui Geological Archive from July 2015 to July 2020.

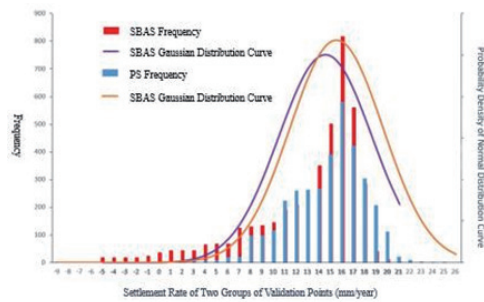


Fig. 15. (Color online) Average annual subsidence rate and normal distribution curve of PS-INSAR and SBAS.

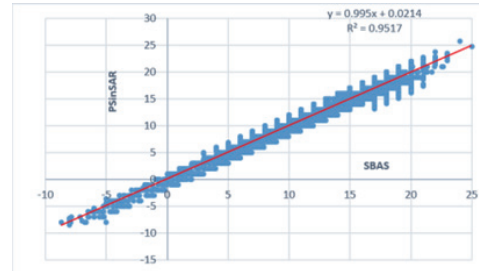


Fig. 16. (Color online) Linear relationship between PS and SBAS annual average subsidence rates.

Fig. 16. This indicates a high degree of consistency between the two methods regarding annual average subsidence rates and verifies the reliability of both methods for monitoring urban land subsidence.⁽²⁵⁾

In conclusion, the four selected regions in the Sentinel-1A data exhibit a consistent linear deformation trend, and the results obtained from both the PSInSAR and SBAS techniques are in agreement. Since the leveling data for the period 2015–2020 in the Heifei area was not available, the accuracy of the land subsidence results obtained using SBAS and PSInSAR techniques cannot be directly verified. However, by comparing and analyzing the results with existing research findings, the reliability of these two temporal InSAR techniques for the accurate monitoring of urban land subsidence in the Heifei area can be indirectly validated. Furthermore, the linear relationship between the annual average subsidence rates calculated by the PSInSAR and SBAS methods provides further confirmation of the accuracy of both methods.

6. Conclusion

In this study, we utilized PSInSAR and SBAS techniques to conduct LOS-based land subsidence monitoring experiments using the near five-year ascending orbit data of Heifei City acquired by Sentinel-1A SAR. The research obtained LOS-based land subsidence information in the study area. The monitoring experiment results revealed that the overall Heifei urban area remains relatively stable, but certain localized regions exhibit deformation trends. Typical areas showing such trends include the Anhui Jiatong Tire Factory, the northern and eastern sections of Heifei South Station's building and nearby railway tracks, university colleges, and the Anhui Provincial Geological Data Museum. The analysis of these four representative regions demonstrates that both PSInSAR and SBAS techniques exhibit characteristics such as high measurement accuracy, wide coverage, and high spatiotemporal resolution. They can provide effective means for the accurate monitoring of large-scale land subsidence in urban areas, offering significant potential for various applications.

On the other hand, there are still some areas for improvement in the current study, including the following: (1) The resolution of Sentinel-1A data is 20×5 m, which allows for obtaining the deformation distribution over a large area. However, higher-resolution SAR data is required for

fine-scale monitoring. (2) Simple sinusoidal function fitting is insufficient to accurately remove periodic deformation signals observed in localized areas. It is necessary to incorporate external data such as temperature and groundwater levels to further optimize the model and achieve the precise removal of periodic signals. (3) The PSInSAR technique primarily measures signals from stable reflectors such as buildings and bridges, making it challenging to capture surface deformation signals in bare land and vegetated areas. This limitation results in the inability to obtain effective measurement signals in certain critical local areas in cities, such as along subway lines. To achieve comprehensive coverage, it is necessary to complement the measurements using the SBAS technique, which can be combined with PSInSAR for monitoring. (4) Although a considerable number of images were used in the experiment, only the ascending orbit data from Sentinel-1A was utilized. Interpreting the results from a single orbit is relatively difficult, and it is necessary to further supplement and process descending orbit data to integrate and interpret both ascending and descending results.

The experiments in this study demonstrate that time-series InSAR monitoring technology performs well in high-precision deformation monitoring. However, it is only aimed at the deformation in the LOS direction. In future applications, it is recommended to use Earth curvature correction and elevation data, and use triangulation to convert the deformation in the LOS direction into vertical displacement. The results should be integrated with the ground measurement data of the Beidou⁽¹⁾ Navigation Satellite System (BDS) to improve the accuracy of monitoring results.

Acknowledgments

This work was supported by the Anhui Provincial Natural Science Foundation under Grant 2108085QD154, the China Postdoctoral Science Foundation under Grant 2020M681993, the National Natural Science Foundation of China under Grant 42001408, and the Natural Science Foundation of Anhui Provincial Education Department under Grant KJ2021A0022.

References

- 1 L. Chaoran, C. Jiehua, L. Donglie, G. Jincheng, D. Jie, and L. Mingsheng: *Nanjing Univ. Inf. Sci.* **12** (2020) 216. <https://doi.org/10.13878/j.cnki.jnuist.2020.02.009>
- 2 B. Chen, H. Gong, Y. Chen, K. Lei, C. Zhou, Y. Si, X. Li, Y. Pan, and M. Gao: *Int. J. Appl. Earth Obs. Geoinf.* **96** (2021) 102284. <https://doi.org/10.1016/j.jag.2020.102284>
- 3 L. Liu, J. Yu, B. Chen, and Y. Wang: *Eur. J. Remote Sens.* **53** (2020) 141. <https://doi.org/10.1080/22797254.2020.1728582>
- 4 F. Hu and J. Wu: *Proc. 2019 6th Asia-Pacific Conf. Synthetic Aperture Radar (IEEE, 2019)* 1–6.
- 5 Z. Zhang, M. Wang, Z. Wu, and X. Liu: *Sensors* **19** (2019) 5306. <https://doi.org/10.3390/s19235306>
- 6 Z. Zeng, Y. Wang, Y. Yan, N. Xiao, and D. Chen: *Proc. IGARSS 2018–2018 IEEE Int. Geoscience and Remote Sensing Symp. (IEEE, 2018)* 4889–4892.
- 7 A. M. Ruiz-Armenteros, J. M. Delgado, B. J. Ballesteros-Navarro, M. Lazecky, M. Bakon, and J. J. Sousa: *Proc. IGARSS 2019–2019 IEEE Int. Geoscience and Remote Sensing Symp. (IEEE, 2019)* 2244–2247.
- 8 B. Zhu, and Y. Wang: *Proc. IGARSS 2019–2019 IEEE Int. Geoscience and Remote Sensing Symp. (IEEE, 2019)* 2006–2009.
- 9 Y. Yan, Y. Wang, and Z. Zeng: *Proc. IGARSS 2018–2018 IEEE Int. Geoscience and Remote Sensing Symp. (IEEE, 2018)* 4885–4888.
- 10 T. Kusunose and J. Susaki: *2021 7th Asia-Pacific Conf. Synthetic Aperture Radar (IEEE, 2021)* 1–6.

- 11 B. Bayer, D. Schmidt, and A. Simoni: IEEE Trans. Geosci. Remote Sens. **55** (2017) 2618. <https://doi.org/10.1109/TGRS.2017.2648885>
- 12 T. Kusunose, J. Susaki, Y. Fujiwara, and H. Hisada: Proc. IGARSS 2022–2022 IEEE Int. Geoscience and Remote Sensing Symp. (IEEE, 2021) 2927–2930.
- 13 A. Tripathi, A. R. Reshi, M. Moniruzzaman, K. R. Rahaman, R. K. Tiwari, and K. Malik: IEEE Sens. J. **22** (2022) 21071. <https://doi.org/10.1109/JSEN.2022.3208117>
- 14 H. Li, L. Zhou, T. Li, X. Wen, X. Shi, and J. Ma: Proc. 2019 6th Asia-Pacific Conf. Synthetic Aperture Radar (IEEE, 2019) 1–5.
- 15 S. A. Huang, J. M. Sauber, and R. Ray: Geophys. Res. Lett. **49** (2022) n/a. <https://doi.org/10.1029/2022GL101363>
- 16 W. Duan, H. Zhang, Y. Tang, C. Wang, X. Zeng, and J. Wang: Proc. 2019 SAR in Big Data Era (IEEE, 2019) 1–4.
- 17 W. Duan, H. Zhang, Y. Tang, C. Wang, X. Zeng, and J. Wang: Proc. IGARSS 2020–2020 IEEE Int. Geoscience and Remote Sensing Symp. (IEEE, 2020) 1993–1996.
- 18 W. Duan, H. Zhang, Y. Tang, C. Wang, X. Zeng, and J. Wang: Proc. 2020 AIAA/IEEE 39th Digital Avionics Systems Conf. (IEEE, 2020) 1–9.
- 19 W. Duan, H. Zhang, Y. Tang, C. Wang, X. Zeng, and J. Wang: Proc. 2021 2nd China Int. SAR Symp. (SISE, 2021) 1–8.
- 20 W. Duan, H. Zhang, Y. Tang, C. Wang, X. Zeng, and J. Wang: Proc. IGARSS 2020–2020 IEEE Int. Geoscience and Remote Sensing Symp. (MDPI AG, 2020) 6670–6673.
- 21 K. Pepin and H. Zebker: Proc. 2021 IEEE Int Geoscience and Remote Sensing Symp. IGARSS (IEEE, 2021) 2663–2666.
- 22 C. Ren, Z. Zhu, L. Zhou, X. Shi, X. Li, and Z. Zhang: Proc. 2019 6th Asia-Pacific Conf. Synthetic Aperture Radar (IEEE, 2019) 1–4.
- 23 Z. Zeng, Y. Wang, D. Chen, and N. Xiao: Proc. EUSAR 2018 12th European Conf. Synthetic Aperture Radar (IEEE, 2018) 1–4.
- 24 J. Takami: Proc. 2021 7th Asia–Pacific Conf. Synthetic Aperture Radar (IEEE, 2021) 1–6.
- 25 Y. Yan, M.-P. Doin, P. Lopez-Quiroz, F. Tupin, B. Fruneau, V. Pinel, and E. Trouve: IEEE J. Sel. Top. Appl. Earth Obs. Remote Sens. **5** (2012) 1312. <https://doi.org/10.1109/JSTARS.2012.2191146>.

About the Authors

Siyuan Liu graduated from Heifei University in 2020 with a bachelor's degree. Since 2021, he has been pursuing a bachelor's degree at Anhui University. His research interests include remote sensing geodesy, machine learning, and remote sensing target detection.

Kai Xu received his Ph.D. degree from Wuhan University (WHU), Wuhan, China in 2017. He is currently an associate professor in Anhui University. His research interests include geometric calibration and image processing using deep learning. (kaixu@ahu.edu.cn)

Chengcheng Fan received his Ph.D. degree from Wuhan University (WHU), Wuhan, China in 2017. He is currently an associate researcher in Innovation Academy for Microsatellites of CAS (IAMCAS). His research interests include remote sensing satellite design and on-orbit intelligent processing.